Editor summary:

This study reports age-dependent negative correlations between temporal changes in maximal leaf area index and growing season length, indicating contrasting leaf acclimation strategies driving vegetation greening in young versus old deciduous broadleaf forests.

Reviewer Recognition:

Nature Plants thanks Rakesh Tiwari and the other, anonymous, reviewer(s) for their contribution to the peer review of this work.

Figure or Table # Please group Extended Data items by type, in sequential order. Total number of items (Figs. + Tables) must not exceed 10.	**Figure/Table title** One sentence only	**Filename** Whole original file name including extension. i.e.: Smith_ED_Fig1.jpg	**Figure/Table Legend** If you are citing a reference for the first time in these legends, please include all new references in the main text Methods References section, and carry on the numbering from the main References section of the paper. If your paper does not have a Methods section, include all new references at the end of the main Reference list.
Choose an item.	None	None	None
Choose an item.			
Choose an item.			
Choose an item.			
Choose an item.			
Choose an item.			
Choose an item.			
Choose an item.			
Choose an item.			
Choose an item.			

13

Item	**Present?**	**Filename** Whole original file name including extension. i.e.: Smith_SI.pdf. The extension must be .pdf	**A brief, numerical description of file contents.** i.e.: *Supplementary Figures 1-4, Supplementary Discussion, and Supplementary Tables 1-4.*

Supplementary Information	Yes	Supplementary_Information.pdf	
Reporting Summary	Yes	Chen Flat RS 0108.pdf	
Peer Review Information	No	*OFFICE USE ONLY*	

14

15

16

17

Type	**Number** **Each type of file (Table, Video, etc.) should be numbered from 1 onwards. Multiple files of the same type should be listed in sequence, i.e.: Supplementary Video 1, Supplementary Video 2, etc.**	**Filename** **Whole original file name including extension. i.e.: *Smith_ Supplementary_Video_1.mov***	**Legend or Descriptive Caption** **Describe the contents of the file**
Choose an item.	None	None	None
Choose an item.			
Choose an item.			
Choose an item.			
Choose an item.			
Choose an item.			

Parent Figure or Table	**Filename** **Whole original file name including extension. i.e.: *Smith_SourceData_Fig1.xls,* or *Smith_ Unmodified_Gels_Fig1.pdf***	**Data description** **i.e.: Unprocessed western Blots and/or gels, Statistical Source Data, etc.**
Source Data Fig. 1	None	None
Source Data Fig. 2		
Source Data Fig. 3		
Source Data Fig. 4		
Source Data Fig. 5		
Source Data Fig. 6		
Source Data Fig. 7		
Source Data Fig. 8		
Source Data Extended Data Fig./Table 1		
Source Data Extended Data Fig./Table 2		
Source Data Extended Data Fig./Table 3		
Source Data Extended Data Fig./Table 4		
Source Data Extended Data Fig./Table 5		

Source Data Extended Data Fig./Table 6		
Source Data Extended Data Fig./Table 7		
Source Data Extended Data Fig./Table 8		
Source Data Extended Data Fig./Table 9		
Source Data Extended Data Fig./Table 10		

19

Title

Contrasting age-dependent leaf acclimation strategies driving vegetation greening across deciduous broadleaf forests in the middle to high latitudes

Author list

Fangyi Wang[1,#], Meimei Xue[1,#], Liming Zhou[2], Christopher E. Doughty[3], Philippe Ciais[4], Peter B. Reich[5,6], Jiali Shang[7], Jing Ming Chen[8], Jane Liu[8], Julia K. Green[3], Dalei Hao[9], Shengli Tao[10], Yanjun Su[11], Lingli Liu[11], Jianyang Xia[12], Han Wang[13], Kailiang Yu[14], Zaichun Zhu[15], Peng Zhu[16], Xing Li[1], Hui Liu[17], Yelu Zeng[18], Kai Yan[19], Liyang Liu[4], Raffaele Lafortezza[20], Yongxian Su[21], Yanqiong Meng[22], Yixuan Pan[1], Xueqin Yang[1], Yongshuo H. Fu[19], Nianpeng He[23], Wenping Yuan[24], Xiuzhi Chen[1,*]

Those authors contribute equally.

* Corresponding authors: X. Chen (chenxzh73@mail.sysu.edu.cn)

Affiliations

1. Guangdong Province Data Center of Terrestrial and Marine Ecosystems Carbon Cycle, School of Atmospheric Sciences, Sun Yat-sen University, Zhuhai, China;
2. Department of Atmospheric and Environmental Sciences, University at Albany, State University of New York, Albany, NY 12222, USA;
3. School of Informatics, Computing, and Cyber Systems, Northern Arizona University, Flagstaff, AZ, USA;
4. Laboratoire des Sciences du Climat et de l'Environnement, IPSL, CEA-CNRS-UVSQ, Université Paris-Saclay, Gif sur Yvette, France;
5. Institute for Global Change Biology and School for Environment and Sustainability, University of Michigan; Ann Arbor, USA;
6. Department of Forest Resources, University of Minnesota; St. Paul, USA;
7. Ottawa Research and Development Centre, Agriculture and Agri-Food Canada, Ottawa, Ontario, Canada;
8. Department of Geography and Planning, University of Toronto, Toronto, Ontario, Canada;
9. Atmospheric Sciences and Global Change Division, Pacific Northwest National Laboratory, Richland, WA, USA;
10. Institute of Ecology, Peking University, Beijing, China;
11. State Key Laboratory of Vegetation and Environmental Change, Institute of Botany, Chinese Academy of Sciences, Beijing, China
12. School of Ecological and Environmental Sciences, East China Normal University, Shanghai 200241, PR China;
13. Department of Earth System Science, Ministry of Education Key Laboratory for Earth System Modeling, Institute for Global Change Studies, Tsinghua University, Beijing 100084, China;
14. Institute of Geographical Sciences and Natural Resources Research, Chinese Academy of Sciences; Beijing, China

15. School of Urban Planning and Design, Peking University, Beijing, China;
16. School of Biological Sciences, The University of Hong Kong, Hong Kong, China;
17. South China Botanical Garden, Chinese Academy of Sciences, Guangzhou, China;
18. College of Land Science and Technology, China Agricultural University, Beijing, China;
19. Center for GeoData and Analysis, State Key Laboratory of Remote Sensing Science, Faculty of Geographical Science, Beijing Normal University, Beijing, China;
20. Department of Agricultural and Environmental Sciences, University of Bari "A. Moro", Bari, Italy;
21. State Key Laboratory of Urban and Regional Ecology, Research Center for Eco-Environmental Sciences, Chinese Academy of Sciences, Beijing, China;
22. School of Forestry and Landscape Architecture, Anhui Agricultural University, Hefei 230036, China;
23. School of Forestry, Northeast Forestry University, Harbin 150040, China;
24. College of Urban and Environmental Sciences, School of Urban Planning and Design, Peking University, Beijing, China.

Abstract

Increasing leaf area and extending vegetation growing seasons are two primary drivers of global greening, which has emerged as one of the most significant responses to climate change. However, it remains unclear how these two leaf acclimation strategies would vary across forests at a large spatial scale. Using multiple satellite-based datasets and field measurements, we analyzed the temporal changes (Δ) in maximal leaf area index (LAI_{max}) and length of the growing season (LOS) from 2002 to 2021 across deciduous broadleaf forests (DBFs) in the middle to high latitudes. Contrary to the widely held assumption of coordination, our results revealed a negative correlation between ΔLAI_{max} and ΔLOS. Notably, the trade-offs between ΔLAI_{max} and ΔLOS were strongly explained by stand age. Younger DBFs, with lower baseline LAI_{max}, predominantly located in eastern Asia, displayed an increase in LAI_{max} with small changes in *LOS*. This acquisitive strategy facilitated younger DBFs to grow more photosynthetically efficient leaves with low leaf mass per area, enhancing their light-use efficiency. Conversely, older DBFs with a higher baseline LAI_{max}, primarily located in North America and Europe, extended their *LOS* by increasing leaf mass per area. This conservative strategy facilitated older DBFs to produce thicker, but less-photosynthetically efficient leaves, resulting in decreased light-use efficiency. Our findings offer new insights into the contrasting changes in leaf area and growing season length and highlight their divergent impacts on ecosystem functioning.

Main

In recent decades, vegetation greening, defined as the increase of annual or seasonal vegetation greenness observed by satellites, has become one of the most significant responses of plants to climate change [1-3]. This global greening encompasses a range of leaf acclimation strategies among plants worldwide, which have not been fully understood. One commonly observed strategy is to produce more canopy leaves[4,5],

while another is to adapt the timing of the growing season, either by advancing its start (*SOS*)[6,7] and/or delaying its end (*EOS*)[8,9]. The first strategy leads to an increase in maximum leaf area index (LAI_{max})[10,11], while the second results in an increase in the length of the growing season (*LOS*= *EOS* - *SOS*)[12-15]. A fundamental question has been whether and how these two leaf acclimation strategies vary across biomes under climate change.

Satellite observations have recorded increases in LAI_{max} and *LOS* across deciduous broadleaf forests (DBFs)[4,7,16-20]. The widely held belief is that LAI_{max} and *LOS* have changed coordinatively. Nevertheless, according to the leaf economics spectrum theory, leaf trait trade-offs often occur within and among plant communities[21,22]. Plants located at the 'fast' end of economics spectrum tend to produce thinner and more efficient leaves with a shorter lifespan, yielding a faster return on investment in terms of carbon gain relative to the resources invested in leaf construction, while plants located at the 'slow' end of the economics spectrum tend to adopt a conservative strategy and favor less efficient leaves with a longer leaf lifespan[21,23,24]. In this context, young forests are expected to adopt an acquisitive strategy to grow more leaves for maximizing carbon gain under climate change[22,25]. In contrast, old forests may follow a conservative strategy, prioritizing *LOS* extension to maximize photosynthesis over time[22,25]. Based on this viewpoint, we hypothesize that forests at different growth stages respond differently to climate change (i.e., increasing LAI_{max} or extending *LOS*). Although this reasoning is conceptually appealing, it has not yet been fully examined in the real world at large spatial scales. Addressing these knowledge gaps can enhance our understanding of the complex leaf acclimation strategies in response to climate change and their implications for ecosystem functioning (i.e., productivity).

We leveraged multiple satellite-based datasets (**Supplementary Table 1**) and field measurements to investigate the LAI_{max} versus *LOS* acclimation strategies and their potential controls by stand age (denoted as A_{age}) at large spatial scales. We focused exclusively on DBFs in the middle to high latitudes (**Supplementary Fig. 1**, section 1 in **Methods**), which exhibit a *LOS* of less than 12 months and moderate LAI (typically LAI < 6.0 m^2 m^{-2}). Thus, LAI metric in this biome shows less saturation problem and is sensitive to vegetation density[26,27]. We first examined the correlations between decadal changes in LAI_{max} (defined as the average *LAI* between the maturity and senescence period, **Supplementary Fig. 2**) and in *LOS* (defined as the average *LOS* between the green-up and dormancy period) (denoted, respectively, as ΔLAI_{max} and ΔLOS) using satellite-based GLASS LAI product[28] and MODIS leaf phenology dataset[29] during 2002-2021 (section 2 in **Methods**). Then, we used satellite-derived leaf moisture content (LMC) (2002-2016)[30] and leaf mass per area (*LMA*) estimated from MODIS reflectance data[31-33] via the PROSAIL model[34,35] to investigate potential changes in leaf traits alongside variations in LAI_{max} and LOS. Satellite observations were validated against field measurements of *LMA* and *LMC* from the widely referenced TRY Plant Trait database[36,37]. Finally, we assessed the cascading impacts on light use efficiency (*LUE*), defined as the ratio of gross primary production (GPP) to absorbed photosynthetically active radiation (APAR) using data-driven GPP from BESS (v2.0), PAR from GLASS (04B01.V60), and the fraction of absorbed PAR

(fAPAR) from GLASS (09B01.V60)[38-40].

Results

Negative correlation between ΔLAI_{max} and ΔLOS

We found that DBFs displayed contrasting patterns in ΔLAI_{max} and ΔLOS during the period 2002-2021, with a small but significant negative linear correlation (R = -0.16; $P < 0.001$) (**Fig. 1a-c**). Overall, DBFs with LOS extensions (ΔLOS > 5.0 days) were primarily located in North America (32%) and Europe (16%) (**Fig. 1b**), together accounting for 48% of the study areas. In contrast, 39% of the studied DBFs showed an increase in LAI_{max} (ΔLAI_{max} > 0.1 m^2 m^{-2}), mostly clustered in eastern Asia (22.22%) and scattered across Europe (3%) (**Fig. 1a**).

Interestingly, the negative relationship between ΔLAI_{max} and ΔLOS was strongly explained by stand age (A_{age}), with ΔLAI_{max} sharply decreasing (slope = -1.73×10^{-3} m^2 m^{-2} $year^{-1}$) and ΔLOS increasing (slope = 7.85×10^{-2} days $year^{-1}$) as A_{age} increased (**Fig. 1d,e**). Younger DBFs with a lower baseline LAI_{max} maintained a larger $A_{leaf}/A_{sapwood}$ ratio, representing the ratio of total leaf area (A_{leaf}) to the sapwood cross-sectional area ($A_{sapwood}$)[43,44] (**Supplementary Fig. 3b,c)**. Consequently, younger DBFs in Asia with smaller A_{age} could afford a substantial increase in LAI_{max} (**Fig. 1a**). In contrast, older DBFs with higher baseline LAI_{max} showed a relatively lower $A_{leaf}/A_{sapwood}$ ratio (**Supplementary Fig. 3b,c**). As a result, older DBFs in North America and Europe with larger A_{age} appeared to produce less additional leaf growth (**Fig. 1a**). Instead, they markedly advanced the *SOS* and/or delayed the *EOS* (**Supplementary Fig. 4**), resulting in a notable increase in *LOS* (**Fig. 1b**).

Changes in leaf physics and chemistry

ΔLAI_{max} and ΔLOS can be associated with different changes in the physical and chemical properties of leaves across DBFs with varying A_{age}. *LMA* is a leaf trait highly related to leaf chemical properties such as nitrogen, phosphorus, and potassium content[46]. Therefore, we explored the temporal changes in *LMA* (ΔLMA) during the period 2002-2016 and used ΔLMA as a proxy to investigate leaf chemical variability across DBFs with different A_{age}. Additionally, we assessed the temporal changes in *LMC* (ΔLMC) during the period 2002-2016 based on the time-series MODIS-derived *LMC* datasets[30] and used ΔLMC as a proxy to examine leaf physical variability (refer to sections 4-5 in **Methods** for details).

We found that both ΔLMA and ΔLMC were positively correlated with A_{age} ($P < 0.001$) (**Fig. 2**). Specifically, younger forests in eastern Asia (regionally averaged A_{age} = 54.29 ± 0.14 years) showed decreases in *LMA* by 1.39 mg cm^{-2} and in *LMC* by 1.18% during the study period (**Supplementary Fig. 5**). This suggested that, with ongoing climate change, younger DBFs tended to produce more, thinner leaves with lower LMC. Conversely, older DBFs exhibited larger positive ΔLMA and ΔLMC values (**Fig. 2b, d**). For instance, in North America and Europe, where the regionally averaged A_{age} was 77.23 years, *LMA* increased by 1.27 mg cm^{-2} and 1.94 mg cm^{-2}, while *LMC* increased by 5.55% and 8.72%, respectively (**Supplementary Fig. 5**). These results indicated that older DBFs tended to develop thicker leaves with higher *LMC*, promoting leaf longevity under climate change. The satellite-based results were

further validated using field observations of specific leaf area (*SLA*) and leaf dry matter content (*LDMC*) from the TRY dataset[36,37] (**Supplementary Fig. 6;** section 6 in **Methods**), where *SLA* is the reciprocal of *LMA,* and *LDMC* is complementary to *LMC*, respectively[47,48]. These analyses also showed negative correlations between *SLA*, *LDMC*, and A_{age}, aligning with the satellite-inferred findings (**Fig. 2b,d**).

Overall, the contrasting changes in leaf properties between younger and older DBFs were associated with the age-dependent negative correlations between ΔLAI_{max} and ΔLOS.

Implications for ecosystem functioning

The contrasting changes in leaf physical and chemical properties between younger and older DBFs can lead to cascading effects on ecosystem photosynthesis. To examine this, we quantified temporal changes in LUE (ΔLUE) over the 2002-2016 period and used structural equation modeling (SEM) to investigate the main paths through which leaf traits (*LMA* versus *LMC*) might impact *LUE* (**Fig. 3a,b**). To eliminate the impacts of climate variability, we applied the SEM analyses within each 2°×2° moving window and calculated the regionally averaged path coefficient (R_{pc}) of ΔLMA versus ΔLMC impact on ΔLUE (**Fig. 3c**).

Results indicated that decreases in *LMA*, usually alongside the increase in canopy leaves, primarily enhanced *LUE* (R_{pc} = -0.117). For instance, younger forests in eastern Asia (**Fig. 3a**), where leaf acclimation favored thinner leaves (**Fig. 4a**), exhibited a substantial increase in ecosystem LUE (ΔLUE = $2.38 \times 10^{-3} \pm 5.10 \times 10^{-5}$ g C J^{-1}) (**Fig. 3b**). In contrast, older forests, primarily located in North America and Europe (**Fig. 3a**), experienced significant declines in LUE (ΔLUE = $-7.31 \times 10^{-4} \pm 4.12 \times 10^{-5}$ g C J^{-1}) (**Fig. 3b**). These declines were linked to the extension of *LOS* accompanied by widespread increases in ΔLMA (ΔLMA = 1.26 ± 0.02 mg cm^{-2}; R_{pc} = -0.117) and ΔLMC (ΔLMC = 7.12 ± 0.10 %; R_{pc} = -0.142) (**Fig. 3c**). This driving mechanism of leaf physical and chemical changes impact on *LUE*, as illustrated by the SEM analyses, remained robust across various A_{age} bins (**Supplementary Fig. 7**). Overall, younger forests tended to grow thinner leaves with higher photosynthetic efficiency to enhance *LUE*, while older forests tended to develop thicker leaves with a longer lifespan but lower photosynthetic efficiency, leading to reduced *LUE* (**Fig. 4**).

Potential uncertainties and caveats

A key issue to consider is the validity of a dynamic phenological extraction threshold method to extract *LOS*[49]. This approach uses a dynamic threshold of the 2-band Enhanced Vegetation Index (EVI2) to determine the start (*SOS*) and end (*EOS*) of the growing season based on the seasonal cycle of EVI2 data[50]. The EVI2 threshold (denoted as $EVI2_0$ in **Equation 1**) is defined as a linear function of two extreme EVI2 values: $EVI2_{min}$ (the minimum of EVI2) and $EVI2_{max}$ (the maximum of EVI2). While $EVI2_{min}$ remains relatively stable, $EVI2_{max}$ varies annually and can influence the value of $EVI2_0$, leading to uncertainties in *LOS* estimation ($\Delta LOS_{uncertainty}$) (refer to section 2 in **Methods** for details). Specifically, $EVI2_{max}$ increases in the case of greening and may cause a rise in $EVI2_0$, leading to an overall shorter *LOS* ($\Delta LOS_{uncertainty} < 0$).

This may artificially introduce a negative correlation between ΔLOS ($\Delta LOS < 0$) and ΔLAI_{max} ($\Delta LAI_{max}>0$). Therefore, accounting for uncertainties associated with the dynamic *LOS* extraction threshold method is crucial for confirming the robustness of the satellite-observed contrasting changes in LAI_{max} and LOS. To address this, we first applied a dynamic phenological threshold to the EVI2 curve to reproduce the MODIS phenology product (**Supplementary Fig. 8a, b**). Second, we quantified $\Delta LOS_{uncertainty}$ associated with changes in EVI2$_{max}$ ($\Delta EVI2_{max}$) (section 2 in **Methods**). As expected, the dynamic phenological threshold method could result in negative correlations between $\Delta EVI2_{max}$and $\Delta LOS_{uncertainty}$, but such impacts are overall minor (**Supplementary Fig. 8c, d**). By subtracting $\Delta LOS_{uncertainty}$ from the corresponding ΔLOS for each pixel, results still showed a significant ($P < 0.001$) negative relationship between ΔLAI_{max} and ΔLOS (**Supplementary Fig. 8f**). We further used fixed EVI2 thresholds (0.2, 0.25 and 0.30) to extract *SOS* and *EOS*, which were then used to compute *LOS*. The observed negative relationship between ΔLAI_{max} and ΔLOS still held true (**Supplementary Fig. 9**).

To minimize impacts from interannual data variability, we examined the negative correlations between ΔLAI_{max} and ΔLOS across different time frames, randomly selected for each pixel**.** These analyses further confirmed the robustness of our findings regarding this negative relationship (**Supplementary Fig. 10)**. Additionally, we calculated the slope of the linear correlation between the time-series of LAI_{max} (slope$_{LAImax}$), *LOS* (slope$_{LOS}$), and time (also known as a linear trend or temporal trend). The results also showed negative correlations between slope$_{LAImax}$ and slope$_{LOS}$ (**Supplementary Fig. 11**). These analyses showed that the contrasting changes in LAI_{max} and LOS reflected a biological reality rather than an artifact of a specific phenological extraction method or random temporal variability.

Uncertainties may also arise from tree cover changes, which can influence both the sign and magnitude of ΔLAI_{max}. To address this, we classified DBFs into four groups based on their tree cover fraction: 50%-60%, 60%-70%, 70%-80%, and >80%. For each group, we analyzed the relationship between ΔLAI_{max} and ΔLOS within different tree cover change bins (0-1%, 1%-2%, 2%-3%, 3%-4%, 4%-5%). Results consistently showed negative correlations between ΔLAI_{max} and ΔLOS across all tree cover change bins, confirming the robustness of our findings (**Supplementary Fig. 12**). Extreme climate events may also introduce uncertainties. For instance, our analysis showed that droughts could reduce ΔLAI_{max}, which in turn weakened the negative correlations between ΔLAI_{max} and ΔLOS (**Supplementary Fig. 13**). Under drought conditions, the acclimation of leaf chemical and physical properties played a less important role in regulating light use efficiency (**Supplementary Fig. 14**).

Furthermore, correlations between ΔLAI_{max} and ΔLOS may vary across tree species. To examine this, we analyzed field-observed phenological data of the USA National Phenology Network[51] (**Supplementary Fig. 15**), the Pan European Phenological database[52] (**Supplementary Fig. 16**), and the northern Eurasia Phenological database[53] (**Supplementary Fig. 17**) against the MODIS EVI product at a higher resolution of 250 m[54] (see section 3 in **Methods**). Results showed that field-observed ΔLOS in most species remained positively correlated with A_{age}. The

ΔEVI_{max} also exhibited a negative correlation with ΔLOS. However, the relationship between ΔEVI_{max} and A_{age} may vary considerably across species.

Overall, while the negative ΔLAI_{max}-ΔLOS relationship observed in this study is generally robust, uncertainties remain due to limitations in field-based *LAI* and leaf trait data, the coarse resolution of satellite observations, and the complexity of forest communities across local to global scales.

Discussion

A key finding of this study is the contrasting changes in leaf area and growing season length in deciduous broadleaf forests across various stand age. While climate change has driven widespread global greening[4], it remains unexplored at large scales whether increases in maximal leaf area[4,5] and extension in growing seasons coordinate or trade off with each other[55-58]. Here, we observed that younger forests with a lower baseline LAI favor the growth of additional thinner leaves[59-61]. In contrast, older forests with a higher baseline LAI prioritize extensions of growing season length over additional leaf growth[62,63]. This finding enhances our understanding of global vegetation greening and highlights the necessity of considering different leaf acclimation strategies (i.e., growing new leaves versus extending growing season longevity) when modelling the foliar phenological shifts under climate change.

The divergent changes in leaf properties identified in this study align with the classic leaf economics spectrum theory, which emphasizes such trade-offs[21,22]. Younger forests located at the 'fast' end of the economics spectrum tended toward an acquisitive strategy[22,25]. With climate change, these forests produced more thinner leaves with a lower percent water content, constraining the extension of growing season and shifting canopy towards higher photosynthetic capacity leaves[3,64-66]. We showed that forests adopting a 'fast' economics strategy were characterized by an increase in LAI_{max}, accounted for 39% of DBFs in the middle to high latitudes. Conversely, as community succession progressed, forest ecosystems tended to contain more older trees, which may shift toward a more conservative strategy[22,25]. These forests (48% of DBFs) predominantly followed a 'slow' economics strategy, mostly extending their *LOS* by producing thicker leaves with a higher percent water content that could remain on the canopy for longer[47]. Consequently, this acclimation strategy tended to reduce ecosystem *LUE*[67-69].

In summary, we found a negative correlation between changes in maximal leaf area index and growing season length. These contrasting changes were strongly influenced by stand age, reflecting contrasting leaf acclimation between younger and older forests. These strategies led to distinct changes in leaf mass per area and leaf moisture content, with cascading impacts on carbon fluxes. Our findings emphasized the importance of accounting for diverse leaf acclimation strategies to fully understand the relationships among changes in leaf area, growing seasons, leaf physics and leaf chemistry, and their effects on ecosystem functioning under climate change.

Methods

(1) Selecting DBFs without disturbances

Our study focused on DBFs in the middle to high latitudes with a defined leaf lifespan (< 12 months) and moderate leaf area index ($LAI < 6.0\ m^2\ m^{-2}$), which exhibited minimal saturation issues in satellite signals[26,27]. We selected 0.05° resolution grid cells classified as 'deciduous broadleaf forests' with tree cover > 50% in the MODIS MCD12C1 V061 land cover imagery from 2002 to 2021[71]. Notably, we excluded DBFs in tropical forests that may have different climatic drivers from those in mid-to-high latitudes. To minimize the impacts of natural disturbances and land cover changes, we overlaid 30 m high-resolution global tree cover change maps from Global Forest Watch (GFW)[42] onto the 0.05° resolution MODIS land cover images, excluding grid cells with tree cover changes greater than 5% over the study period[72]. We retained only DBF grid cells with consistent land cover type (within 0 ± 0.05 fraction) from 2002 to 2021. To ensure robustness, we controlled tree cover changes within small bins to test our key findings of this study (**Supplementary Fig. 12**). Additionally, we excluded pixels affected by wildfires by removing 0.05° forest grid cells with burned areas during the study period, using the MODIS Fire_cci AVHRR-LTDR Burned Area Pixel product (Version 1.1)[41], which provides a 0.05° spatial and monthly temporal resolution.

Moreover, extreme climatic events like droughts can introduce variability in LAI and phenology. To account for this, we classified the studied DBFs into several drought groups. Pixels that experienced severe drought events were used to assess the impacts of drought on these responses (**Supplementary Fig. 13**). Notably, a month was classified as experiencing severe drought if the anomaly of Palmer Drought Severity Index (PDSI)[73,74] fell more than 1.5 standard deviation below the 2002-2021 monthly mean[75]. A year was considered as a drought year for a given pixel if it experienced four consecutive months of drought between the start (*SOS*) and end (*EOS*) dates of the growing season period (see definition in section 2 of **Methods**). Notably, for each given pixel, we identified the *SOS* and *EOS* for each year and used the multiple-year averaged *SOS* and *EOS* as the time nodes to count the drought events during the study period.

(2) Exploring relationships between ΔLAI_{max} and ΔLOS

We utilized the GLASS LAI (01B01.V60) product (2002-2021)[28], with a spatial resolution of 0.05° and an 8-day temporal resolution, to calculate ΔLAI_{max}. During this period, the GLASS LAI data were derived from MODIS surface reflectance data using the bidirectional LSTM deep learning model[28]. We first downloaded the Maturity_1 and Senescence_1 layers from the MODIS global vegetation characterization product (MCD12Q2, 500 m resolution)[29] via Google Earth Engine at a 0.05° resolution. These layers represented the dates when EVI2 first (leaf maturity) and last (leaf senescence) crossed the 90% of the segment amplitude threshold[29], corresponding to the leaf maturity and senescence stages, respectively. We then calculated the mean *LAI* during this period as LAI_{max} for each pixel (**Supplementary Fig. 2**).

We used the MCD12Q2 phenology products to calculate ΔLOS. The MCD12Q2 phenology products used a dynamic phenological extraction threshold ($EVI2_0$) based on a simple linear function (**Equation 1**) of the minimal ($EVI2_{min}$) and maximal ($EVI2_{max}$) values of $EVI2$ to determine the start (*SOS*) and end (*EOS*) dates of the

growing season[29]:

$$EVI2_0 = EVI2_{min} + 15\% \times (EVI2_{max} - EVI2_{min}) \quad (1)$$

where $EVI2_0$ represents the dynamic threshold of *EVI2* used to identify *SOS* and *EOS*. *SOS* is defined as the day when the $EVI2$ seasonal curve crosses $EVI2_0$ within the green-up segment, while *EOS* is defined as the day when the $EVI2$ curve crosses $EVI2_0$ within the green-down segment.

The layers of Greenup_1 and Dormancy_1 in the MCD12Q2 product (Version 6.1) were produced based on **Equation 1** to represent *SOS* and end *EOS*, respectively. Here we computed the length of the growing season (*LOS*) using **Equation 2**.

$$LOS = EOS - SOS \quad (2)$$

Notably, MCD12Q2 time series after 2012 were corrected using different method as those for the time series before 2012[50], leading to potential discontinuity for *LOS* time series. Thus, in this study, temporal changes in *LOS*, denoted as ΔLOS, were calculated as mean of ΔLOS between the periods 2002-2004 and 2010-2012 and ΔLOS between the periods 2013-2015 and 2019-2021(**Fig. 1b**). The same was done for calculating corresponding ΔLAI_{max} (**Fig. 1a**).

To assess uncertainties caused by interannual data variability, we randomly selected different time frames to calculate ΔLAI_{max} and ΔLOS. Specifically, for each pixel, we used the MATLAB's random number generators to randomly generate pairs of years that were at least five years apart from each other within the study period. Then, we calculated the ΔLAI_{max} and ΔLOS between each randomly selected pairs of years. This random sampling approach was applied to all pixels independently to ensure that the time frame for each pixel was set randomly. Similarly, to mitigate potential impacts from this discontinuity before and after 2012, the random-time-frame-testing was performed for the periods 2002-2012 and 2013-2021, respectively (**Supplementary Fig. 10)**. Additionally, we tested the contrasting change in LAI_{max} and *LOS* with time using temporal trends for the periods 2002-2012 and 2013-2021, respectively (**Supplementary Fig. 11**). The trends of temporal changes in LAI_{max} and *LOS* were defined as the slopes of the linear correlation between time-series of LAI_{max} ($slope_{LAImax}$), LOS ($slope_{LOS}$) and time.

To examine the relationship between ΔLAI_{max} and ΔLOS in DBFs with varying stand age (A_{age}), we used the widely adopted MPI-BGC stand age (A_{age}) dataset at a 1 km spatial resolution[45]. The gridded A_{age} data were derived from a machine learning model trained on over 40,000 forest plots, integrating forest inventory data, biomass, and climate variables[45]. This dataset also accounts for variations in tree cover thresholds through aboveground biomass maps[45]. We then analyzed the changes in $A_{leaf}/A_{sapwood}$, LAI_{max}, *LOS*, leaf properties (*LMA* and *LMC*), and *LUE* with rising A_{age}. The sapwood area ($A_{sapwood}$) data were obtained from Liu et al. (2019)[43] and He et al. (2025)[44], while datasets for other leaf traits, such as *LMA*, *LMC,* and *LUE*, are introduced in the following sections.

Notably, $EVI2_0$ in Equation 1 depends on $EVI2_{min}$ and $EVI2_{max}$. While $EVI2_{min}$ remained relatively stable, $EVI2_{max}$ varied annually, largely influencing the value of $EVI2_0$ and in turn introducing uncertainties in calculating ΔLOS (refer to the first paragraph in "**Potential uncertainties and caveats**" section). In other words, ΔLOS

computed using this method may be inherently related to ΔLAI_{max}[49]. To account for this dependency, we replaced the $EVI2_{max}$ of the starting year with that of the final year within the selected time frame to obtain new *LOS* data for each pixel. The differences between this new and the original *LOS* data were quantified as *LOS* uncertainties ($\Delta LOS_{uncertainty}$) caused by the dynamic phenological extraction threshold method (i.e., changes in $EVI2_{max}$) (**Supplementary Fig. 8**). Furthermore, we also used three fixed EVI2 thresholds (0.2, 0.25, and 0.30) to extract *SOS* and *EOS*, and then *LOS* to test the robustness of the negatively relationship between ΔLAI_{max} and ΔLOS, (**Supplementary Fig. 9**).

(3) Validations using in-situ and high-resolution satellite data

We further validated the robustness of the negative correlations between ΔLAI_{max} and ΔLOS using higher-resolution satellite-based MOD13Q1 v061 EVI[54] (website: https://lpdaac.usgs.gov/products/mod13q1v061/) and field-observed *LOS* data from global phenology networks[51-53] (website: http://www.pep725.eu/; https://doi.org/10.1038/s41597-020-0376-z; https://www.usanpn.org/results/data). The MOD13Q1 EVI dataset (2002-2021) was derived from Terra sensors with a spatial resolution of 250m and a temporal resolution of 16 days[54].

Field-based *LOS* data were calculated using the *EOS* and *SOS* information provided by the Pan European Phenology Network (PEP725)[52], the Russian "Chronicles of Nature" Network (RCNN)[53], and the USA National Phenology Network (USA-NPN)[51]. PEP725 offers over 13 million records for 201 species from 26,000 sites in Europe, with data dating back to 1868[52]. The RCNN provides data from 471 sites across Russia, Ukraine, Uzbekistan, Belarus, and Kyrgyzstan[53], while the USA-NPN includes 3,000 records across the USA[51]. For the European and Russian observation sites, the *SOS* was defined using records coded as "BBCH11", while the *EOS* was defined using codes of "BBCH94". At the USA sites, *SOS* and *EOS* were defined based on records of "Breaking leaf buds" and ">=50% of leaves colored (deciduous)", respectively. The *LOS* was calculated using Equation (2).

Notably, we focused exclusively on DBF observation sites. To ensure the robustness of long-term phenological records, we included sites with more than five years of observations for the random-time-frame analysis in European and Russian observation sites. In contrast, for the USA, where SOS and EOS are generally shorter, we included sites with at least two years of observations. We calculated ΔLOS based on phenological time series records for each genus or species at each observation site. Specifically, ΔLOS was derived by subtracting the *LOS* in the initial year from that in the final year for each species at each site. For each site, we calculated ΔEVI_{max} using data corresponding to the years and time frames used to determine *LOS*. The results are shown in **Supplementary Figs. 15-17**.

(4) Exploring leaf physical, chemical, and functional changes

We used satellite-based leaf moisture content (*LMC*)[30] products and model-derived leaf mass area (*LMA*)[32,33] to examine the temporal changes in leaf physical and chemical properties. The daily *LMC* product (2002-2016) has a spatial resolution of

0.25° and provides global estimates of *LMC* with median, maximum, and minimum values to capture uncertainty. This study used the median *LMC* values for analysis. *LMA* data were derived from canopy-level reflectance measurements from the MODIS MCD43A4 V6.1 (2002-2016) using the PROSPECT-5 and 4SAIL models[32,33,76] (refer to the following section for the **Methods** of PROSPECT modeling of leaf mass area (*LMA*) from satellite-based on canopy-level reflectance). We calculated interannual variability in growing-season (from the Greenup_1 to Dormancy_1 day) *LMA* (ΔLMA) and *LMC* (ΔLMC) between the periods 2002-2004 and 2014-2016 to investigate changes in leaf physical and chemical properties over time.

We calculated temporal changes in growing-season *LUE*, denoted as ΔLUE (the 2014-2016 period minus the 2002-2004 period), to assess their influences on ecosystem functioning. *LUE* was calculated by dividing gross primary production (GPP)[38] by the product of photosynthetically active radiation (PAR)[39] and the fraction of absorbed PAR (fAPAR)[40]. GPP data were derived from the BESSv2.0 model, a satellite-based coupled-process model for estimating global land-atmosphere fluxes[38]. This GPP dataset, with a spatial resolution of 0.05 °, spans from 1982 to 2019, and provides daily cumulative data validated against FLUXNET observations, demonstrating reliable performance across different spatial and temporal scales. The daily PAR and fAPAR data were sourced from the GLASS04B01.V60 and GLASS09B01.V60 products, respectively, both at a 0.05°spatial resolution. All the analysis data were resampled to a 0.05° resolution using bilinear interpolation.

$$LUE = \frac{GPP}{fAPAR \times PAR} \quad (3)$$

(5) Modeling LMA using the PROSAIL model

The PROSPECT-5 model simulates leaf optical properties, specifically reflectance and transmittance across the 400-2500 nm range[76], which includes visible, near-infrared, and shortwave infrared wavelengths that are critical for studying plant physiological properties, based on parameters such as leaf structure (*N,* dimensionless), chlorophyll content (*Cab*), equivalent water thickness (*Cw*), and leaf mass per area (*LMA*)[34]. The 4SAIL model, on the other hand, simulates canopy reflectance, incorporating factors like leaf area index (*LAI*), leaf angle distribution, and soil background[77,78]. The combined PROSAIL model, integrating both PROSPECT-5 and 4SAIL, enables detailed spectral simulations from leaf to canopy levels based on these leaf traits, making it a widely-used tool for studying temporal changes in leaf traits and relative reflectance[76,79]. In this study, we applied the PROSAIL model to derive leaf mass per area (*LMA*) across DBFs in the middle to high latitudes during the 2002-2016 period[80].

First, we input the leaf trait parameters (**Supplementary Table 2**) into the PROSAIL model to simulate leaf-level reflectance across DBFs in the middle to high latitudes from 2002 to 2016. The maximum and minimum values for parameters such as *N*, *LAI*, *Cab*, *LMA*, and *Cw* were primarily derived from remote sensing data and prior knowledge from the literature[78,81-84]. Fixed values were assigned to parameters such as leaf brown pigment and the hot spot size parameter[85,86]. For each set of input parameter values, the PROSAIL model simulated leaf reflectance across the 400 nm -

2500 nm spectrum. Reflectance was then extracted for seven specific spectral bands (visible: 459-479 nm, 545-565 nm, and 620-670 nm; near-infrared: 841-876 nm; shortwave infrared: 1230-1250 nm; 1628-1652 nm, and 2105-2155 nm), matching the MODIS MCD43A4 reflectance imagery bands. This data was used to establish a look-up table (LUT), linking simulated leaf reflectance of the seven spectral bands to corresponding leaf traits such as *LAI*, *Cab*, *LMA*, and *Cw*. Ultimately, 26,124,444 sets of reflectance and leaf traits were generated.

Next, we extracted satellite-observed reflectance for above-mentioned seven spectral bands from the MODIS Nadir BRDF-Adjusted Reflectance (NBAR) product (MCD43A4 V6.1) for each DBF grid cell during the 2002-2016 period. The MCD43A4 V6.1 product provides daily MODIS band 1-7 surface reflectance at 500 m resolution[31]. To ensure data quality, we applied the quality assurance (QA) flag to exclude cloud-affected pixels. The optimal reflectance was determined when the mean squared error between the simulated and observed spectra was minimized, calculated using Equation (4)[87]. The *LMA* corresponding to the optimal reflectance was determined as the model-simulated *LMA* for each DBF grid cell.

$$MSE = \frac{\sum_{\lambda=1}^{n}(R_{measured,i} - R_{LUT,i})^2}{n} \quad (4)$$

where *MSE* is the mean squared error. $R_{measured,i}$ is a measured reflectance at wavelength i and $R_{LUT,i}$ is a modeled reflectance at wavelength i, and n is the number of wavelengths.

(6) Validations using in-situ SLA and LDMC data

We further validated the temporal changes in model-simulated *LMA* and satellite-inferred *LMC* using field-observed specific leaf area (*SLA*) (7855 records) and leaf dry matter content (*LDMC*) (4363 records) data from the TRY database (website: https://www.try-db.org/) (**Supplementary Fig. 6**). *SLA* is the reciprocal of *LMA* and *LDMC* is complementary to *LMC*[47,48]. The TRY database is a global repository containing over 2.88 million entries across approximately 69,000 plant species[36,37]. Due to the lack of long-term time series records for *SLA* and *LDMC* at individual sites, we averaged the site-level *SLA* and *LDMC* within each 2°×2° spatial grid cell, and then calculated ΔSLA and $\Delta LDMC$ by subtracting the *SLA* and *LDMC* values of earlier years from those of later years. Results based on field observations showed contrasting patterns of *SLA* and *LDMC* against A_{age}, consistent with those of model-simulated *LMA* and satellite-inferred *LMC* (black dots and line) (**Fig. 2b and 2d**).

(7) Exploring impacts of ΔLMA and ΔLMC on ΔLUE

This study employed SEM to investigate the paths through which ΔLMA and ΔLMC, along with climatic variability, influenced ΔLUE. The SEMs were constructed using the *lavaan* package in *R*[88]. Path coefficients (R_{pc}) between variables were used to evaluate model fit. Notably, spatial climate variability may also bring uncertain impacts on the ΔLMA-ΔLUE and ΔLMC-ΔLUE relationships in the SEM model. Thus, to eliminate the impacts from spatial climate variability, we applied the SEM modeling analysis within each 2°×2° moving window. The path coefficients in the SEM models

in **Fig. 3** and **Supplementary Figs. 7** and **14** were the average values of corresponding path coefficients in the SEM model applied in each 2°×2° moving window across the selected DBFs. In addition, drought years were excluded from the SEM analysis in **Fig. 3c**, while analysis including the impacts of droughts were shown in **Supplementary Fig. 14** for comparison.

Data Availability

All the relevant data come from publicly available sources. GLASS LAI (01B01.V60) product: http://www.glass.umd.edu/LAI/MODIS/0.05D/; The satellite leaf unfolding and dormancy dates product: https://lpdaac.usgs.gov/products/mcd12q2v061/; The MPI-BGC stand age data through: https://doi.org/10.17871/ForestAgeBGI.2021; The MODIS Nadir BRDF-Adjusted Reflectance (NBAR) products (MCD43A4) is available on Google Earth Engine website: https://developers.google.com/earth-engine/datasets/catalog/MODIS_061_MCD43A4; The leaf moisture content data is obtained from: https://doi.org/10.5281/zenodo.6545571; The BESSv2.0 GPP data is form: https://www.environment.snu.ac.kr/bessv2; GLASS PAR (04B01.V60) product: http://www.glass.umd.edu/PAR/; GLASS fAPAR (09B01.V60) product: http://www.glass.umd.edu/FAPAR/MODIS/0.05D/; Global Land cover data is from https://lpdaac.usgs.gov/products/mcd12c1v061/; The MOD13Q1 V061 EVI data is available at: https://lpdaac.usgs.gov/products/mod13q1v061/. The *in-situ* leaf unfolding date product of Europe, Russia, and the USA, respectively, are obtained from: http://www.pep725.eu, https://doi.org/10.1038/s41597-020-0376-z, https://www.usanpn.org/data/observational; The TRY database is from: https://www.try-db.org/; The MODIS FireCCILT11 (Version 1.1) data is available at: https://catalogue.ceda.ac.uk/uuid/b1bd715112ca43ab948226d11d72b85e/; The GFW Global Forest Change v1.9 data is from: https://glad.earthengine.app/view/global-forest-change. The PDSI data is from: https://climate.northwestknowledge.net/TERRACLIMATE.

Code Availability

The code used for this study is available in a Zenodo repository at https://doi.org/10.5281/zenodo.15765680 (ref. [89]).

Acknowledgments

We thank the three reviewers for their valuable time and constructive comments. This study was supported by the National Natural Science Foundation of China (Nos. 42471326, 31971458, and U21A6001), the National Key R&D Program of China (No. 2024YFF1306600), and the Science and Technology Program of Guangdong (No. 2024B1212070012).

Author Contributions Statement

X.C. designed the study, wrote the initial manuscript, and revised the manuscript.

F.W. and M.X. collected the data, performed the analysis, drew the figures, and wrote the Method section. L.Z., C.-E.D., P.C., P.-B.R., J.S., J.-M.C., J. L., J.-K.G., D.H., S.T., Y.-J.S., L.-L.L., J.X., H.W., K.-L.Y., Z.Z., P.Z., X.L., H.L., Y.Z., K. Yan, L.-Y.L., R.L., Y.-X.S., Y.M., Y.P., X.Y., Y.-H.F., N.H., and W.Y. contributed to discussing the scientific question, writing, and revising the manuscript.

Competing Interests Statement

The authors declare no competing interests.

Figure Captions

Fig. 1 Contrasting changes in maximal leaf area index (ΔLAI_{max}) and length of growing season (ΔLOS) from 2002 to 2021 across deciduous broadleaf forests (DBFs) in the middle to high latitudes. a, Map of ΔLAI_{max} during the 2002-2021 period. **b**, Map of ΔLOS during the 2002-2021 period. **c**, Negative correlation between ΔLAI_{max} and ΔLOS, with the black line representing the linear regression between two variables. The 95% confidence interval (CI) of the Pearson's correlation coefficient (R) in the square brackets was tested by using the Fisher's z-transformation. **d**, Negative correlation between ΔLAI_{max} and stand age (A_{age}). **e**, Positive correlation between ΔLOS and stand age (A_{age}). The black lines in panels **d** and **e** represent the linear regressions between ΔLAI_{max} and A_{age} and between ΔLOS and A_{age}, respectively. A_{age} data were extracted from the widely used MPI-BGC global forest dataset[45]. In panels **c**-**e**, the *P* values were evaluated using a two-sided Student's t-test.

Fig. 2 Temporal changes in leaf mass per area (ΔLMA) and leaf moisture content (ΔLMC) from 2002 to 2016 across deciduous broadleaf forests (DBFs) in the middle to high latitudes. a, Map of ΔLMA during the 2002-2016 period. **b**, Positive correlations between ΔLMA and stand age (A_{age}). The black dots indicate the satellite-based ΔLMA data. The black line represents the linear regressions between ΔLMA and A_{age}. The specific leaf area (*SLA*) is the reciprocal of *LMA*[47]. The brown dots indicate the field-observed ΔSLA data. The brown line represents the linear regressions between ΔSLA and A_{age}. **c**, Map of ΔLMC between the same two periods. **d**, Positive correlations between ΔLMC and A_{age}. The black dots indicate satellite-based ΔLMC data. The black line represents the linear regressions between ΔLMC and A_{age}. The leaf dry matter content (*LDMC*) is complementary to *LMC*[48]. The blue dots indicate the field-observed $\Delta LDMA$ data. The blue line represents the linear regressions between $\Delta LDMC$ and A_{age}. The field-observed ΔSLA and $\Delta LDMC$ were both evaluated within each 2°×2° grid cell. (refer to sections 4-6 in **Methods** for details). In panels **b** and **d**, the *P* values were calculated using a two-sided Student's t-test.

Fig. 3 Cascading influences on changes in ecosystem light use efficiency (ΔLUE) from 2002 to 2016 across deciduous broadleaf forests (DBFs) in the middle to high latitudes. a, Map of ΔLUE during the 2002-2016 period. **b**, Negative correlation between A_{age} and ΔLUE. The black line represents the linear regression between

ΔLUE and A_{age}. The P values were calculated using a two-sided Student's t-test. **c**, Structural equation modeling (SEM) of the paths of changes in leaf physical and chemical properties (ΔLMA and ΔLMC) impacting ΔLUE. The path coefficients were the average values of corresponding path coefficients in the SEM model applied in each 2°×2° moving window across the selected DBFs.

Fig. 4 Schematic representation of age-dependent leaf acclimation strategies driving vegetation greening across deciduous broadleaf forests (DBFs) in the middle to high latitudes. **a**, Younger DBFs tend to develop thinner, and more photosynthetically efficient leaves. **b**, Older DBFs tend to extend the growing season with thicker, but less-photosynthetically efficient leaves.

References

1. Guo, K. et al. Leaf morphogenesis: The multifaceted roles of mechanics. *Molecular Plant*, **15**, 1098–1119 (2022).
2. Liu, J. et al. Evidence for widespread thermal acclimation of canopy photosynthesis. *Nature Plants*, **10**, 1919–1927 (2024).
3. Piao, S. et al. Leaf onset in the northern hemisphere triggered by daytime temperature. *Nature Communications*, **6**, 6911 (2015).
4. Zhu, Z. et al. Greening of the Earth and its drivers. *Nature Climate Change*, **6**, 791–795 (2016).
5. Jian, D. et al. Limited driving of elevated CO2 on vegetation greening over global drylands. *Environmental Research Letters*, **18**, 104024 (2023).
6. Buitenwerf, R., Rose, L., & Higgins, S. I. Three decades of multi-dimensional change in global leaf phenology. *Nature Climate Change*, **5**, 364–368 (2015).
7. Chen, C. et al. China and India lead in greening of the world through land-use management. *Nature Sustainability*, **2**, 122–129 (2019).
8. Wu, C. et al. Contrasting responses of autumn-leaf senescence to daytime and night-time warming. *Nature Climate Change*, **8**, 1092–1096 (2018).
9. Chen, C. et al. Biophysical impacts of Earth greening largely controlled by aerodynamic resistance. *Science advances*, **6**, eabb1981 (2020).
10. Xia, J. et al. Joint control of terrestrial gross primary productivity by plant phenology and physiology. *Proceedings of the National Academy of Sciences*, **112**, 2788–2793 (2015).
11. Huang, K. et al. Enhanced peak growth of global vegetation and its key mechanisms. *Nature Ecology & Evolution*, **2**, 1897–1905 (2018).
12. Zhu, W. et al. Extension of the growing season due to delayed autumn over mid and high latitudes in North America during 1982–2006. *Global Ecology and Biogeography*, **21**, 260–271 (2012).
13. Fu, Y. H. et al. Declining global warming effects on the phenology of spring leaf unfolding. *Nature*, **526**, 104–107 (2015).
14. Wu, C. et al. Contrasting responses of autumn-leaf senescence to daytime and night-time warming. *Nature Climate Change*, **8**, 1092–1096 (2018).
15. Zani, D. et al. Increased growing-season productivity drives earlier autumn leaf

senescence in temperate trees. *Science*, **370**, 1066–1071 (2020).
16. Menzel, A., & Fabian, P. Growing season extended in Europe. *Nature*, **397**, 659 (1999).
17. Gunderson, C. A. et al. Forest phenology and a warmer climate – growing season extension in relation to climatic provenance. *Global Change Biology*, **18**, 2008–2025 (2012).
18. Liu, Q. et al. Extension of the growing season increases vegetation exposure to frost. *Nature Communications*, **9**, 426 (2018).
19. Wang, X. et al. No trends in spring and autumn phenology during the global warming hiatus. *Nature Communications*, **10**, 2389 (2019).
20. Piao, S. et al. Characteristics, drivers and feedbacks of global greening. *Nature Reviews Earth & Environment*, **1**, 14–27 (2020).
21. Reich, P. B., Walters, M. B., & Ellsworth, D. S. Leaf life-span in relation to leaf, plant, and stand characteristics among diverse ecosystems. *Ecological Monographs*, **62**, 365–392 (1992).
22. Wright, I. J. et al. The worldwide leaf economics spectrum. *Nature*, **428**, 821–827 (2004).
23. Reich, P. B., Walters, M. B., & Ellsworth, D. S. From tropics to tundra: Global convergence in plant functioning. *Proceedings of the National Academy of Sciences*, **94**, 13730–13734 (1997).
24. Reich, P. B., & Flores-Moreno, H. Peeking beneath the hood of the leaf economics spectrum. *New Phytologist*, **214**, 1395–1397 (2017).
25. Chazdon, R. L. Beyond deforestation: restoring forests and ecosystem services on degraded lands. *Science*, **320**, 1458–1460 (2008).
26. Yan, K. et al. Performance stability of the MODIS and VIIRS LAI algorithms inferred from analysis of long time series of products. *Remote Sensing of Environment*, **260**, 112438 (2021).
27. Gao, S. et al. Evaluating the saturation effect of vegetation indices in forests using 3D radiative transfer simulations and satellite observations. *Remote Sensing of Environment*, **295**, 113665 (2023).
28. Ma, H., & Liang, S. Development of the GLASS 250-m leaf area index product (version 6) from MODIS data using the bidirectional LSTM deep learning model. *Remote Sensing of Environment*, **273**, 112985 (2022).
29. Friedl, M., Gray, J., & Sulla-Menashe, D. MODIS/Terra+ Aqua Land Cover Dynamics Yearly L3 Global 500 m SIN Grid V061. *NASA EOSDIS Land Processes DAAC* https://doi.org/10.5067/MODIS/MCD12Q2.061 (2022).
30. Forkel, M. et al. Estimating leaf moisture content at global scale from passive microwave satellite observations of vegetation optical depth. *Hydrology and Earth System Sciences*, **27**, 39–68. (2023).
31. Schaaf, C. & Wang, Z. MODIS/Terra+Aqua BRDF/Albedo Nadir BRDF Adjusted Ref Daily L3 Global - 500m V061. *NASA EOSDIS Land Processes DAAC* https://doi.org/10.5067/MODIS/MCD43A4.061 (2021).

32. Féret, J.-B. et al. T. Estimating leaf mass per area and equivalent water thickness based on leaf optical properties: Potential and limitations of physical modeling and machine learning. *Remote Sensing of Environment*, **231**, 110959 (2019).
33. Sun, J. et al. Analyzing the performance of PROSPECT model inversion based on different spectral information for leaf biochemical properties retrieval. *ISPRS Journal of Photogrammetry and Remote Sensing*, **135**, 74–83 (2018).
34. Jacquemoud, S., & Baret, F. PROSPECT: A model of leaf optical properties spectra. *Remote Sensing of Environment*, **34**, 75–91 (1990).
35. Jacquemoud, S. et al. Estimating leaf biochemistry using the PROSPECT leaf optical properties model. *Remote Sensing of Environment*, **56**, 194–202 (1996).
36. Kattge, J. et al. TRY – a global database of plant traits. *Global Change Biology*, **17**, 2905–2935 (2011).
37. Kattge, J. et al. TRY plant trait database – enhanced coverage and open access. *Global Change Biology*, **26**, 119–188 (2020).
38. Li, B. et al. BESSv2.0: A satellite-based and coupled-process model for quantifying long-term global land–atmosphere fluxes. *Remote Sensing of Environment*, **295**, 113696 (2023).
39. Zhang, X. et al. Generating Global Land Surface Satellite incident shortwave radiation and photosynthetically active radiation products from multiple satellite data. *Remote Sensing of Environment*, **152**, 318–332 (2014).
40. Ma, H. et al. Global land surface 250-m 8-day Fraction of Absorbed Photosynthetically Active Radiation (FAPAR) product from 2000 to 2020. *Earth System Science Data*, **14**, 5333–5347 (2022).
41. Chuvieco, E., Pettinari, M.L., & Otón, G. ESA Fire Climate Change Initiative (Fire_cci): AVHRR-LTDR Burned Area Pixel product, version 1.1. *Centre for Environmental Data Analysis* https://dx.doi.org/10.5285/b1bd715112ca43ab948226d11d72b85e (2020).
42. Potapov, P. et al. The global 2000-2020 land cover and land use change dataset derived from the Landsat archive: first results. *Frontiers in Remote Sensing*, **3**, 856903 (2022).
43. Liu, F. et al. Variations in orthotropic elastic constants of green Chinese Larch from pith to sapwood. *Forests*, **10**, 456 (2019).
44. He, P. et al. Growing-Season Precipitation Is a Key Driver of Plant Leaf Area to Sapwood Area Ratio at the Global Scale. *Plant, Cell & Environment*, **48**, 746-755 (2025).
45. Besnard, S. et al. Mapping global forest age from forest inventories, biomass and climate data. *Earth System Science Data Discussions*, **2021**, 1-22 (2021).
46. Kikuzawa, K., & Lechowicz, M. J. Ecology of leaf longevity. *Springer Science & Business Media*, (2011).
47. Poorter, H. et al. Causes and consequences of variation in leaf mass per area (LMA): a meta-analysis. *New Phytologist*, **182**, 565–588 (2009).
48. Wang, Z. et al. Leaf water content contributes to global leaf trait relationships. *Nature Communications*, **13**, 5525 (2022).
49. Zhang Y. et al. Autumn canopy senescence has slowed down with global warming

since the 1980s in the Northern Hemisphere. *Communications Earth & Environment*, **4**, 173 (2023).
50. Gray, J., Sulla-Menashe, D., & Friedl, M. A. User guide to collection 6 modis land cover dynamics (mcd12q2) product. *NASA EOSDIS Land Processes DAAC*, **6,** 1-8 (2019).
51. Schwartz, M. D., Betancourt, J. L., & Weltzin, J. F. From Caprio's lilacs to the USA national phenology network. *Frontiers in Ecology and the Environment*, **10**, 324-327 (2012).
52. Templ, B. et al. Pan European Phenological database (PEP725): a single point of access for European data. *International Journal of Biometeorology*, **62**, 1109–1113 (2018).
53. Ovaskainen, O. et al. Chronicles of nature calendar, a long-term and large-scale multitaxon database on phenology. *Scientific Data*, **7**, 47 (2020).
54. Didan, K. MODIS/Terra Vegetation Indices 16-Day L3 Global 250m SIN Grid V061. *NASA EOSDIS Land Processes DAAC* https://doi.org/10.5067/MODIS/MOD13Q1.061 (2021).
55. Gill, A. L. et al. Changes in autumn senescence in northern hemisphere deciduous trees: A meta-analysis of autumn phenology studies. *Annals of Botany*, **116**, 875–888 (2015).
56. Jeong, S.-J. et al. Phenology shifts at start vs. end of growing season in temperate vegetation over the Northern Hemisphere for the period 1982–2008. *Global Change Biology*, **17**, 2385–2399 (2011).
57. Menzel, A. et al. European phenological response to climate change matches the warming pattern. *Global Change Biology*, **12**, 1969–1976 (2006).
58. Piao, S. et al. Variations in satellite-derived phenology in China's temperate vegetation. *Global Change Biology*, **12**, 672–685 (2006).
59. Asshoff, R., Zotz, G., & Körner, C. Growth and phenology of mature temperate forest trees in elevated CO_2. *Global Change Biology*, **12**, 848–861 (2006).
60. Norby, R. J. et al. Net primary productivity of a CO_2-enriched deciduous forest and the implications for carbon storage. *Ecological Applications*, **12**, 1261–1266 (2002).
61. Norby, R. J. et al. Fine-root production dominates response of a deciduous forest to atmospheric CO_2 enrichment. *Proceedings of the National Academy of Sciences of the United States of America*, **101**, 9689–9693 (2004).
62. Fang, K.et al**.** Influence of non-climatic factors on the relationships between tree growth and climate over the Chinese Loess Plateau. *Global and Planetary Change*, **132**, 54-63 (2015).
63. Xu, L.et al. Productivity and water use efficiency of *Pinus tabulaeformis* responses to climate change in the temperate monsoon region. *Agricultural and Forest Meteorology*, **327**, 109188 (2022).
64. Niinemets, Ü. Components of leaf dry mass per area–thickness and density–alter leaf photosynthetic capacity in reverse directions in woody plants. *The New Phytologist*, **144**, 35-47 (1999).
65. Thomas, S. C., & Winner, W. E. Photosynthetic differences between saplings and

adult trees: an integration of field results by meta-analysis. *Tree Physiology*, **22**, 117–127 (2002).
66. Niinemets, Ü., & Sack, L. Structural determinants of leaf light-harvesting capacity and photosynthetic potentials. *Progress in Botany*, 385–419 (2006).
67. Yoshimoto, M., Oue, H., & Kobayashi, K. Energy balance and water use efficiency of rice canopies under free-air CO2 enrichment. *Agricultural and Forest Meteorology*, **133**, 226–246 (2005).
68. Ainsworth, E. A., & Rogers, A. The response of photosynthesis and stomatal conductance to rising [CO_2]: mechanisms and environmental interactions. *Plant, Cell & Environment*, **30**, 258–270 (2007).
69. Zhang, S. et al. Tree species mixing can amplify microclimate offsets in young forest plantations. *Journal of Applied Ecology*, **59**, 1428–1439 (2022).
70. Wang, S. et al. Recent global decline of CO_2 fertilization effects on vegetation photosynthesis. *Science*, **370**, 1295–1300 (2020).
71. Friedl, M. & Sulla-Menashe, D. MODIS/Terra+Aqua Land Cover Type Yearly L3 Global 0.05Deg CMG V061. *NASA EOSDIS Land Processes DAAC* https://doi.org/10.5067/MODIS/MCD12C1.061 (2022).
72. Su, Y. et al. Asymmetric influence of forest cover gain and loss on land surface temperature. *Nature Climate Change*, **13**, 823–831 (2023).
73. Abatzoglou, J. T. et al. TerraClimate, a high-resolution global dataset of monthly climate and climatic water balance from 1958-2015. *Scientific Data*, **5**, 170191 (2018).
74. Wang, X. et al. A two-fold increase of carbon cycle sensitivity to tropical temperature variations. *Nature*, **506**, 212-215 (2014).
75. Liu, L. et al. Tropical tall forests are more sensitive and vulnerable to drought than short forests. *Global Change Biology*, **28**, 1583-1595 (2022).
76. Wang, S. et al. A TPE based inversion of PROSAIL for estimating canopy biophysical and biochemical variables of oilseed rape. *Computers and Electronics in Agriculture*, **152**, 350-362 (2018).
77. Verhoef, W. Light scattering by leaf layers with application to canopy reflectance modeling: The SAIL model. *Remote Sensing of Environment*, **16**, 125-141 (1984).
78. Verhoef, W., & Bach, H. Coupled soil–leaf-canopy and atmosphere radiative transfer modeling to simulate hyperspectral multi-angular surface reflectance and TOA radiance data. *Remote Sensing of Environment*, **109**, 166-182 (2007).
79. Doughty, C. E. et al. Tropical forest leaves may darken in response to climate change. *Nature Ecology & Evolution*, **2**, 1918–1924 (2018).
80. Jacquemoud, S., & Ustin, S. Leaf optical properties. *Cambridge University Press* (2019).
81. Feret, J. et al. PROSPECT-4 and 5: Advances in the leaf optical properties model separating photosynthetic pigments. *Remote Sensing of Environment*, **112**, 3030–3043 (2008).
82. Jacquemoud, S. et al. PROSPECT Plus SAIL models: A review of use for vegetation characterization. *Remote Sensing of Environment*, **113**, S56–S66 (2009).
83. Darvishzadeh, R. et al. Inversion of a radiative transfer model for estimating

vegetation LAI and chlorophyll in a heterogeneous grassland. *Remote Sensing of Environment*, **112**, 2592–2604 (2008).
84. Mousivand, A. et al. Global sensitivity analysis of the spectral radiance of a soil–vegetation system. *Remote Sensing of Environment*, **145**, 131–144 (2014).
85. Breunig, F. M. et al. Spectral anisotropy of subtropical deciduous forest using MISR and MODIS data acquired under large seasonal variation in solar zenith angle. *International Journal of Applied Earth Observation and Geoinformation*, **35**, 294–304 (2015).
86. Yin, C. et al. Chlorophyll content estimation in arid grasslands from Landsat-8 OLI data. *International Journal of Remote Sensing*, **37**, 615-632 (2016).
87. Darvishzadeh, R. et al. Inversion of a radiative transfer model for estimating vegetation LAI and chlorophyll in a heterogeneous grassland. *Remote Sensing of Environment*, **112**, 2592-2604 (2008).
88. Rosseel, Y. lavaan: An R package for structural equation modeling. *Journal of Statistical Software*, **48**, 1-36 (2012).
89. Wang, F. Code to support 'Contrasting age-dependent leaf acclimation strategies driving vegetation greening across deciduous broadleaf forests in the middle to high latitudes'. Zenodo. https://doi.org/10.5281/zenodo.15765680 (2025).

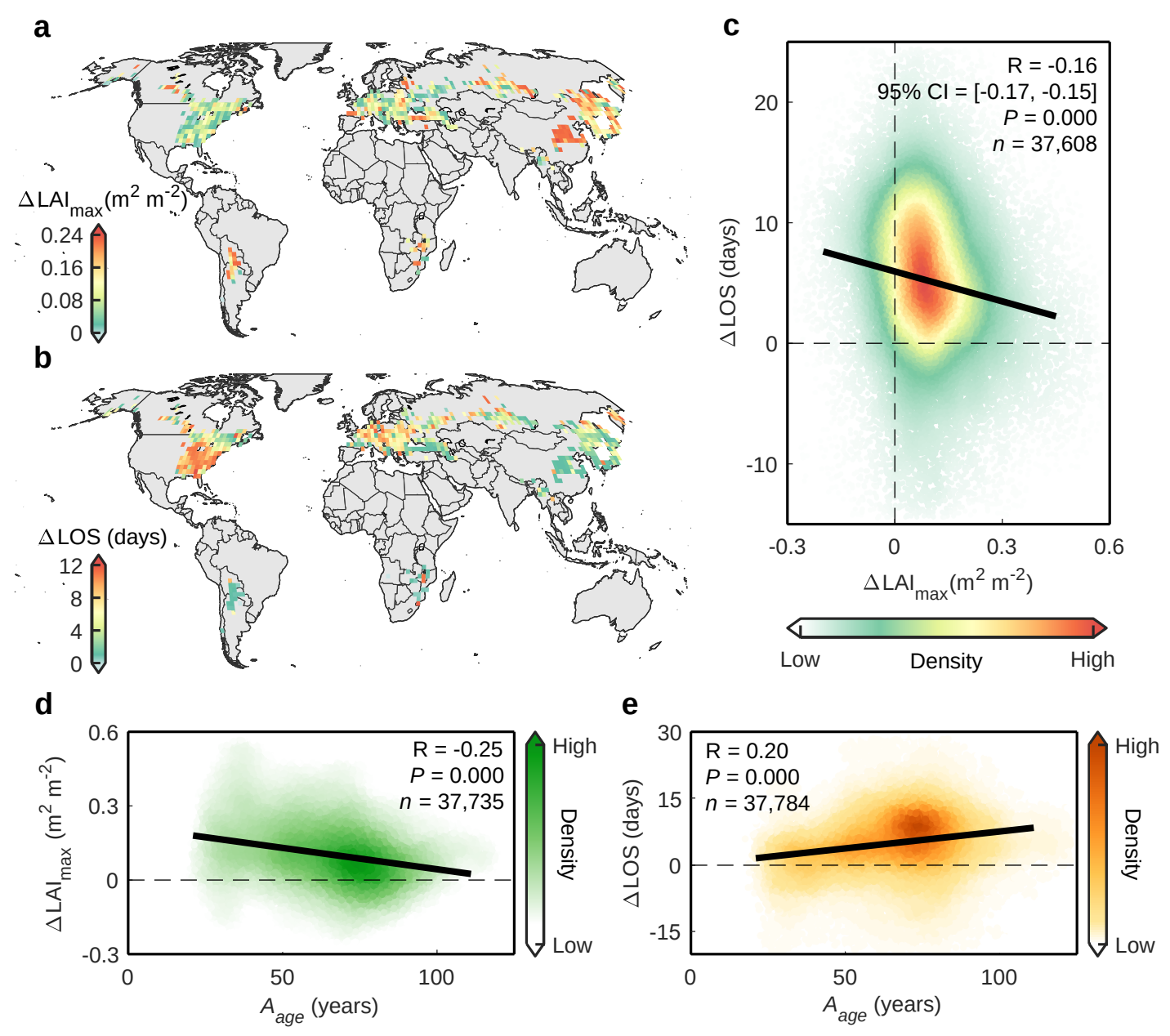
a
ΔLAImax(m2 m-2)
0.24
0.16
0.08
0
b
ΔLOS (days)
12
8
4
0
c
R = -0.16
95% CI = [-0.17, -0.15]
P = 0.000
n = 37,608
ΔLOS (days)
20
10
0
-10
-0.3
0
0.3
0.6
ΔLAImax(m2 m-2)
Low
Density
High
d
R = -0.25
P = 0.000
n = 37,735
ΔLAImax (m2 m-2)
0.6
0.3
0
-0.3
0
50
100
Aage (years)
High
Density
Low
e
R = 0.20
P = 0.000
n = 37,784
ΔLOS (days)
30
15
0
-15
0
50
100
Aage (years)
High
Density
Low

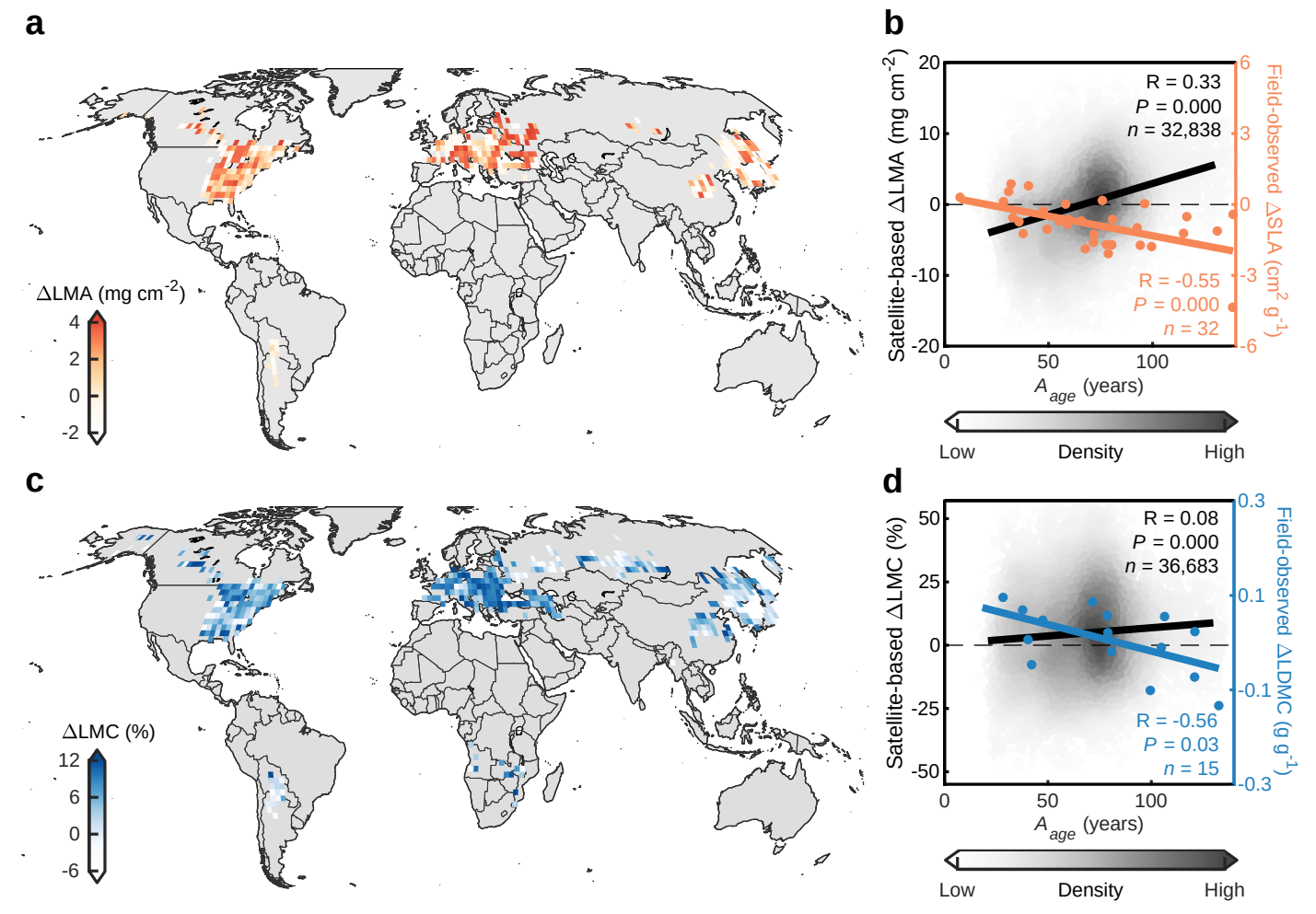
a
ΔLMA (mg cm-2)
4
2
0
-2
b
Satellite-based ΔLMA (mg cm-2)
Field-observed ΔSLA (cm2 g-1)
R = 0.33
P = 0.000
n = 32,838
R = -0.55
P = 0.000
n = 32
20
10
0
-10
-20
6
3
0
-3
-6
0
50
100
Aage (years)
Low
Density
High
c
ΔLMC (%)
12
6
0
-6
d
Satellite-based ΔLMC (%)
Field-observed ΔLDMC (g g-1)
R = 0.08
P = 0.000
n = 36,683
R = -0.56
P = 0.03
n = 15
50
25
0
-25
-50
0.3
0.1
-0.1
-0.3
0
50
100
Aage (years)
Low
Density
High

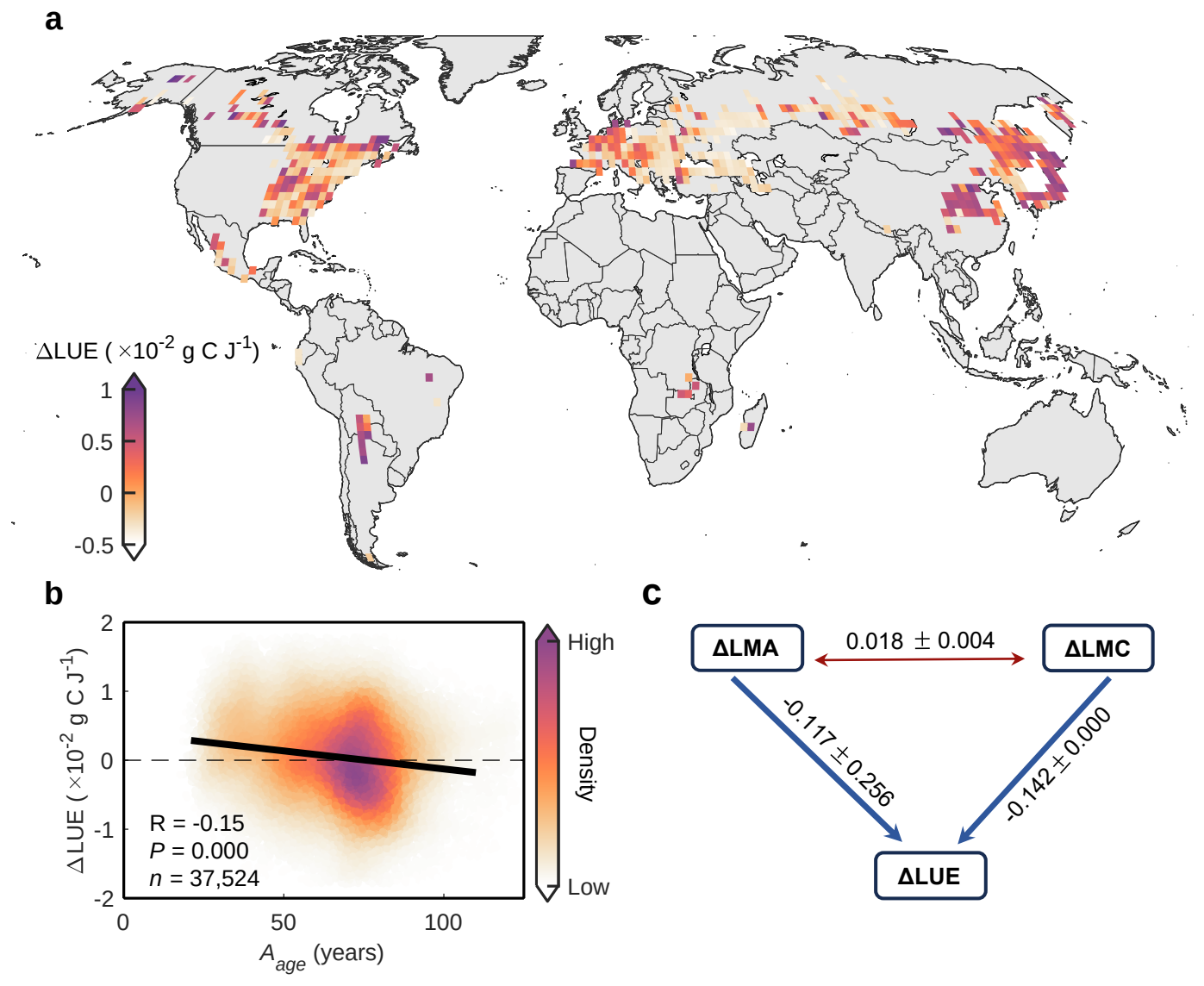
a
ΔLUE (×10-2 g C J-1)
1
0.5
0
-0.5
b
ΔLUE (×10-2 g C J-1)
2
1
0
-1
-2
R = -0.15
P = 0.000
n = 37,524
0
50
100
Aage (years)
High
Density
Low
c
ΔLMA
0.018 ± 0.004
ΔLMC
-0.117±0.256
-0.142±0.000
ΔLUE

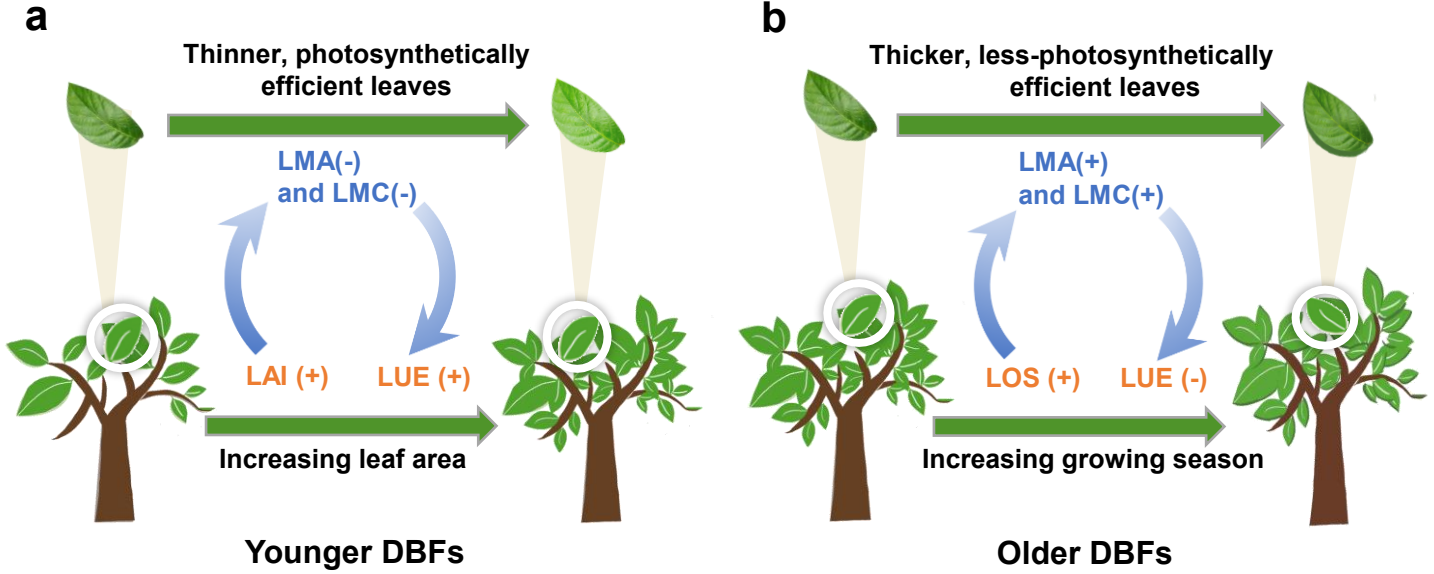
a
Thinner, photosynthetically efficient leaves
LMA(-) and LMC(-)
LAI (+)
LUE (+)
Increasing leaf area
Younger DBFs
b
Thicker, less-photosynthetically efficient leaves
LMA(+) and LMC(+)
LOS (+)
LUE (-)
Increasing growing season
Older DBFs